

# Adaptive Tube Model Predictive Control of Micro- and Nanoparticles in Fluid Suspensions using Global External Fields

Juan Wu and Kaiyan Yu

**Abstract**—An adaptive tube model predictive control (MPC) scheme is presented to manipulate multiple micro- and nanoparticles in fluid suspensions. The control strategy addresses coupled input actuation from the global electric field and estimates the unknown parameters of system dynamics. With the proposed control law, the manipulability of the electrophoresis-based microfluidic manipulation system is quantified and analyzed. The manipulability is affected by the dimensions of the actuating electrodes, the number of particles to be simultaneously and independently controlled, and the configurations of those particles. The scalability of the lattice-shaped distributed array is discussed. Experimental results validate the performance of the control scheme and the manipulability analysis.

## I. INTRODUCTION

The scalable manufacturing of functional micro- and nanodevices has been explored widely in various application areas [1], [2]. The manipulation of micro- and nanoparticles provides more solutions for future manufacturing challenges. Techniques such as optical tweezers [3], magnetic tweezers [4], electric tweezers [5] and tip-based methods [6] are commonly used to steer micro- and nano-objects. In this work, we use electric field-based methods because they are less costly, superior in scalability, and easier to implement for the simultaneous motion control of micro- and nanoparticles [5], [7]–[10]. However, the global and coupled nature of the wireless external field limits the capability to robustly control multiple small-scale particles independently and simultaneously [11].

Without loss of generality, we focus on manipulating micro- and nanoparticles with global DC electric fields. Under DC fields, particles in fluid suspension experience the electrophoresis (EP) and the electro-osmosis (EO) disturbance [7]. However, because of the lack of precise knowledge of the boundary conditions, exact modeling of EP and EO actuation is difficult. As shown in [12], the EO-induced disturbances are not always aligned with the electric field direction because of the complicated boundary conditions, and the existing models of the EO flow cannot be directly applied to our application. Another challenge is caused by the uncontrolled variations existing in system dynamics. The mobilities (i.e., the zeta potentials) of particles in a fluid suspension are unknown and may have various signs and magnitudes. Zeta potentials may vary by orders of magnitude, even though the particles have the same composition, similar shapes and sizes, and are from the same sample [13].

This work was supported by State University of New York Research Seed Grant Program and the Integrated Electronics Engineering Center.

J. Wu and K. Yu are with the Department of Mechanical Engineering, Binghamton University, Binghamton, NY 13902 USA (email: jwu123@binghamton.edu; kyu@binghamton.edu.)

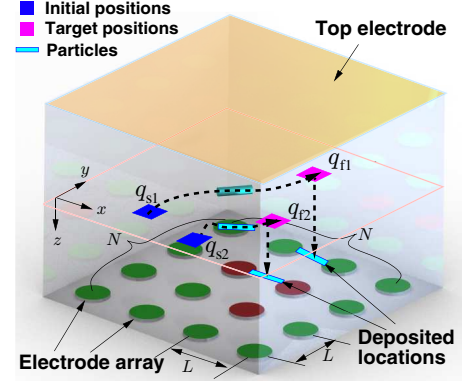


Fig. 1. Schematic of the microfluidic device with  $N \times N$  independently actuated electrodes on the bottom substrate and a common top electrode. The array of circular electrodes with diameter  $L/2$  is fabricated with equal distances  $L$  between the electrode centers as measured along the  $x$  and  $y$  axes. Each electrode is independently actuated with a DC voltage.

Considering the modeling uncertainties of the EO flow and the unknown zeta potentials, we design an adaptive tube model predictive control scheme that describes the EP driving force, makes online estimates of the unknown parameters, and simultaneously compensates for the EO-induced motion disturbance as reported in [14], [15]. The tube MPC is a robust strategy that incorporates the input constraints for nonlinear problems [16]. The strategy requires building fixed-shaped virtual tubes that move along a desired, online generated nominal trajectory [17]. However, preconstructed tubes need a priori knowledge of each particle's zeta potential and the tube geometry is restricted for all operating conditions, which can lead to suboptimal performance [18]. The adaptive control law is combined with the tube MPC approach, so the system uncertainties can be captured online and the state-dependent tubes are updated to potentially reduce the conservativeness of robust MPC while providing robust stability guarantees [19].

Fig. 1 is a schematic of the microfluidic channel in which we steer multiple particles. A generic array of  $N \times N$  lattice-shaped distributed electrodes is fabricated on the bottom of the fluid channel. The proposed adaptive tube MPC estimates the unknown mobilities of the particles, constructs lower-dimension dynamic tubes online, and addresses the challenge of the coupled actuation from the global electric field. Complementing with our previous work in [14], [15], this paper provides comprehensive analyses, extensive simulations, and well-characterized experiments regarding the manipulability based on the tube MPC design.

The main contributions of the work are as follows. (1) We formulate lower-dimension tubes for multiple particles to reduce the computational cost while satisfying the coupled input constraint. Different from the controller design in [14], [15], when manipulating multiple particles, the zeta potentials of each particle are estimated individually, so multiple particles with positive and negative zeta potentials can be controlled independently and simultaneously. (2) We quantify the system's manipulability and discover strong relationships of the manipulability with the dimension of the microfluidic device, the number of particles to be controlled, and the particles' configurations. Those analyses give insights into designing the most effective electrode array to achieve agile particle motions and provide heuristics in the informed motion planning algorithms to find the most achievable trajectories for multiple particles. Experimental results validate the manipulability analyses and the performance of the control strategy.

## II. ADAPTIVE TUBE MPC

In this section, we briefly introduce the adaptive tube MPC. The lower-dimension tube construction process and the online generated reference trajectory are the same as described in [14]. However, the parameter estimation method that relies on estimating one parameter set that contains all the unknowns is modified to one that builds different parameter sets for every individual particle. By separating the parameter estimation for each particle, we can manipulate multiple particles with different signs of zeta potentials. In [14], [15], the unknown zeta potentials are restricted to the same signs. With the new estimation method in this paper, the restriction is removed.

The EP-based motion model of multiple particles in a viscous fluid under an external DC electric field is formatted as the following nonlinear, discrete-time system [14], [15]:

$$\mathbf{q}_{t+1} = \mathbf{A}\mathbf{q}_t + \boldsymbol{\theta}\mathbf{B}(\mathbf{q}_t)\mathbf{u}_t + \mathbf{w}_t, \quad (1)$$

in which  $t$  is the discrete-time index and the state  $\mathbf{q}_t$  is the position vector of all particles at time step  $t$ .  $\mathbf{A}$  is an identity matrix,  $\mathbf{B}(\mathbf{q}_t)$  is the motion gain matrix at the state  $\mathbf{q}_t$ , and  $\boldsymbol{\theta}$  is the zeta potential matrix to be estimated.  $\mathbf{u}_t$  and  $\mathbf{w}_t$  are the control input and the external disturbance at time step  $t$ , respectively. The state and input constraints are given by  $\mathbf{q}_t \in \mathbb{Q}$ ,  $\mathbf{u}_t \in \mathbb{U}$ . We assume that the disturbance  $\mathbf{w}_t$  lies in a convex and compact polytope  $\mathbb{W}$ , where  $\mathbb{W} = \{\mathbf{w}_t : \mathbf{F}_w\mathbf{w}_t \leq \mathbf{f}_w\}$ .

We construct the tube and estimate the zeta potentials for each particle by modifying Eq. (1) to one that applies to each individual particle:  $\mathbf{q}_{t+1}^i = \mathbf{A}^i\mathbf{q}_t^i + \boldsymbol{\theta}^i\mathbf{B}^i(\mathbf{q}_t^i)\mathbf{u}_t + \mathbf{w}_t^i$ .

### A. Parameter Estimation

At time step  $t$ , for  $i$ th particle, the current state  $\mathbf{q}_t^i$  can be obtained through the microscope camera by using an image processing algorithm. An auxiliary set  $\Delta_t^i$  is defined as follows:  $\Delta_t^i = \{\boldsymbol{\theta}^i : -\mathbf{F}_w^i\boldsymbol{\theta}^i\mathbf{B}^i(\mathbf{q}_{t-1}^i)\mathbf{u}_{t-1} \leq \mathbf{f}_w^i - \mathbf{F}_w^i(\mathbf{q}_t^i - \mathbf{A}^i\mathbf{q}_{t-1}^i)\} = \{\boldsymbol{\theta}^i : \mathbf{F}_{\boldsymbol{\theta}^i}^i\boldsymbol{\theta}^i \leq \mathbf{f}_{\boldsymbol{\theta}^i}^i\}$ , in which  $\mathbf{F}_{\boldsymbol{\theta}^i}^i = -\mathbf{F}_w^i\text{diag}(\mathbf{B}^i(\mathbf{q}_{t-1}^i)\mathbf{u}_{t-1})$  and  $\mathbf{f}_{\boldsymbol{\theta}^i}^i = \mathbf{f}_w^i - \mathbf{F}_w^i\mathbf{q}_t^i + \mathbf{F}_w^i\mathbf{A}^i\mathbf{q}_{t-1}^i$ . The  $i$ th estimated parameter set is initialized to be  $\Theta_0^i = \{\boldsymbol{\theta}^i : \mathbf{F}_0^i\boldsymbol{\theta}^i \leq \mathbf{f}_0^i\}$ , and at each time step  $t$ , the set is defined as

$\Theta_t^i = \{\boldsymbol{\theta}^i : \mathbf{F}_t^i\boldsymbol{\theta}^i \leq \mathbf{f}_t^i\}$ , where  $\mathbf{F}_t^i$  and  $\mathbf{f}_t^i$  are changing online. Then, the parameter set is updated by  $\Theta_t^i = \Theta_{t-1}^i \cap \Delta_t^i$ . As a result, for all  $t \in \mathbb{N}$ ,  $\Theta_{t+1}^i \subseteq \Theta_t^i$  holds.

### B. Optimized Dynamic Tubes

An appropriate characterization of a family of robust control invariant (RCI) sets for the *unconstrained*  $i$ th particle's motion is given by  $\mathbf{R}_k^i(\mathbf{M}_k^i) \triangleq \bigoplus_{m=0}^{k-1} \mathbf{D}_m^i(\mathbf{M}_k^i)\mathbb{W}$ , with the following constraints  $\mathbf{D}_k^i(\mathbf{M}_k^i) = \mathbf{0}$  and  $\mathbf{B}^i(\mathbf{q}_t^i)\mathbf{M}_k^j = \mathbf{0}$ , when  $i \neq j$ . The first constraint helps the system reject the external disturbance in  $k$  steps, and the second constraint avoids the coupled input effect from the  $i$ th particle to the  $j$ th particle. The feedback law  $\boldsymbol{\nu}$  is formulated as follows:  $\boldsymbol{\nu}^*(\mathbf{q}_t) \triangleq [\mathbf{M}_{k-1}^1, \dots, \mathbf{M}_0^1]\mathbf{w}^{1*} + [\mathbf{M}_{k-1}^2, \dots, \mathbf{M}_0^2]\mathbf{w}^{2*} + \dots + [\mathbf{M}_{k-1}^n, \dots, \mathbf{M}_0^n]\mathbf{w}^{n*}$ . The tube sets  $[\mathbf{R}_k^{1*}(\mathbf{M}_k^1), \dots, \mathbf{R}_k^{n*}(\mathbf{M}_k^n)]$  satisfy  $\mathbf{R}_k^{i*}(\mathbf{M}_k^i) \subseteq \alpha_i^*\mathbb{Q}$ ,  $i = 1, \dots, n$ . The feedback control law  $\boldsymbol{\nu}^*(\mathbf{q}_t)$  satisfies  $\boldsymbol{\nu}^*(\mathbf{q}_t) \in \mathbf{U}(\mathbb{M}_k) \subseteq n\beta^*\mathbb{U}$ , where  $\mathbf{U}(\mathbb{M}_k) \triangleq \bigoplus_{i=1}^n \mathbf{U}^i(\mathbf{M}_k^i)$ .

### C. Nominal System Controller

The nominal trajectory is generated by solving a finite-horizon, optimal control problem defined as

$$\begin{aligned} \min_{\mathbf{z}, \mathbf{v}} \quad & \sum_{k=0}^{N_h-1} (\|\mathbf{z}_k - \mathbf{q}_f\|_Q^2 + \|\mathbf{v}_k\|_R^2), \\ \text{subject to} \quad & \mathbf{z}_{k+1} = \mathbf{A}\mathbf{z}_k + \boldsymbol{\theta}_{\text{est}}\mathbf{B}(\mathbf{z}_k)\mathbf{v}_k, \\ & \mathbf{z}_k \in \mathbb{Z}, \mathbf{v}_k \in \mathbb{V}, \mathbf{z}_{N_h} \in \mathbb{Z}_f, \end{aligned} \quad (2)$$

where  $\mathbf{z}$  is the state of the nominal system, and  $\mathbf{v}$  is the input of the nominal system.  $Q$  and  $R$  are weight matrices that are set as identity matrices with suitable dimensions.  $\mathbb{Z}$  and  $\mathbb{V}$  are computed subsets based on tube formulation. The optimal control problem leads to the state sequence and the control sequence shown as follows:  $\mathbf{Z}^*(\mathbf{q}_t) = [\mathbf{z}_0^*(\mathbf{q}_t), \mathbf{z}_1^*(\mathbf{q}_t), \dots, \mathbf{z}_{N_h}^*(\mathbf{q}_t)]$  and  $\mathbf{V}^*(\mathbf{q}_t) = [\mathbf{v}_0^*(\mathbf{q}_t), \mathbf{v}_1^*(\mathbf{q}_t), \dots, \mathbf{v}_{N_h-1}^*(\mathbf{q}_t)]$ . With the above solutions, we have the corresponding optimal dynamic tube  $\mathbf{Q}^i(\mathbf{q}_t^i) \triangleq \mathbf{z}_0^*(\mathbf{q}_t^i) \oplus \mathbf{R}_k^i(\mathbf{M}_k^i)$ ,  $i = 1, \dots, n$  and the control policy  $\mathbf{u}_t \triangleq \mathbf{v}_0^*(\mathbf{q}_t) + \boldsymbol{\nu}^*(\mathbf{q}_t)$ .

## III. MANIPULABILITY DISCUSSION

To quantify the ability to manipulate multiple particles with the  $N \times N$  electrode array in the microfluidic device, we define the manipulability similar to Yoshikawa's manipulability index [20] as  $\mu(\mathbf{q}) = d(\mathbf{q})\sqrt{\det(\mathbf{B}(\mathbf{q})\mathbf{B}(\mathbf{q})^T)}$ , where  $d(\mathbf{q})$  is the maximum disturbance that the control law can reject at configuration  $\mathbf{q}$ , and  $\mathbf{B}(\mathbf{q})$  is the motion gain matrix in the system dynamics. Based on the analysis in [15], we further explore the relationships of the manipulability with the configurations and the number of the controlled particles. The center-to-center (CC) distance  $L$  between two adjacent electrodes in the  $N \times N$  electrode array also affects the manipulability of the controlled particles.

### A. Dimension analysis

We denote the cells formed by the  $2 \times 2$  electrodes as atomic cells. Fig. 2 shows the maximum manipulability for controlling one particle in an atomic cell for different CC distances of the

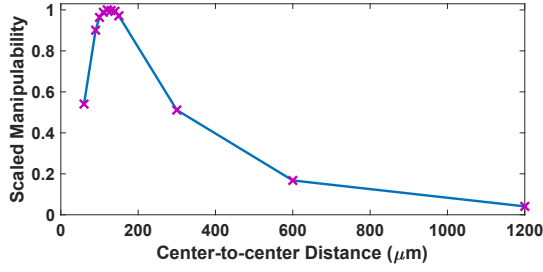


Fig. 2. Scaled maximum manipulability of one particle in an atomic cell for devices with different dimensions.

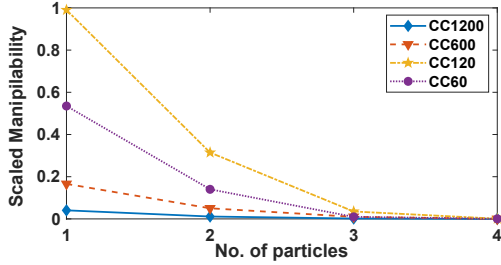


Fig. 3. Scaled maximum manipulability magnitude for simultaneously controlling different numbers of particles in electrode arrays with four dimensions.

arrays. For a better comparison, the maximum manipulabilities of devices with different dimensions are scaled. From the plot, the device with  $L = 120 \mu\text{m}$  (CC120) achieves the largest manipulability, and the maximum manipulability in one atomic cell increases as the CC distance increases until it reaches  $120 \mu\text{m}$ . Then, the maximum manipulability drops as the CC distance increases.

This result matches what we expect because when  $L$  is small, the electric field strength is large, but the electrode boundaries have a large influence on the electric field in the workspace, narrowing the range of possibilities for manipulation. When  $L$  becomes larger, the boundary effect from the electrodes is smaller, but the electric field strength decreases. The CC120 pattern has the best balance between the two factors. When  $L < 120 \mu\text{m}$ , the electrodes' boundary effect takes a dominant effect on the manipulability. When  $L > 120 \mu\text{m}$ , the electric field strength contributes more to the manipulability. This finding will assist with the electrode pattern design to agilely, precisely and efficiently control particles.

#### B. Number of particles to be manipulated

We show the maximum manipulability for steering different numbers of particles in the microfluidic devices with different dimensions in Fig. 3. The manipulabilities are normalized by the maximum value. The manipulability under constraint satisfaction is greatly affected by the number of particles. When the number of controlled particles increases, the ability of the global field for arbitrary manipulation of the particles decreases dramatically. When the number of particles exceeds two, the manipulability drops almost down to zero despite the CC distance of the electrode array. As a result, up to two particles can be put in one atomic cell to maintain the agile manipulation of both particles.

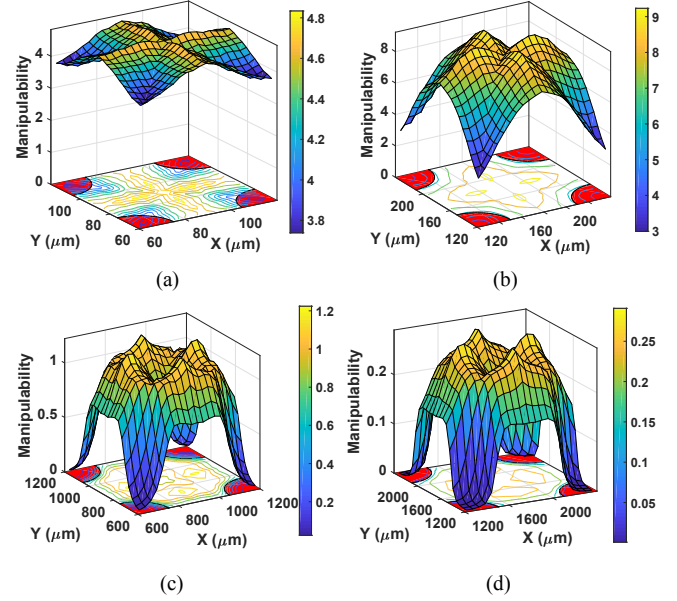


Fig. 4. Manipulability for controlling one particle in one atomic cell of the electrode array with different CC dimensions. The control step is  $\delta t = 0.1 \text{ s}$ . (a) CC60. (b) CC120. (c) CC600. (d) CC1200.

#### C. Configuration analysis

Fig. 4 shows the simulation results of the manipulability for one particle in the center atomic cell with different electrode array dimensions. Particles at different positions in the center atomic cell have different manipulability, and the positions close to the electrodes offer lower manipulability than the center of the atomic cell. To achieve agile and precise manipulation in the atomic cell, the particle should be away from the boundary of the electrodes by at least  $0.1L$ .

In the simulation, we compare the electrode arrays with four dimensions: CC60, CC120, CC600, and CC1200. In one atomic cell of the microfluidic devices with different dimensions, the maximum manipulability seems to appear at similar configurations, and the manipulability distributions have similar shapes, but the magnitudes of the maximum manipulability vary. The simulation results show that the CC60 device has a maximum manipulability of 4.833, and the electrode array of CC120 can achieve manipulability up to 9.229. The maximum manipulability of the CC600 device is 1.223 and the CC1200 device is only 0.2908.

Because we can only agilely manipulate two particles in one atomic cell, we analyze the manipulability against different configurations for two particles in one atomic cell. Fig. 5 shows the numerical simulation results in a CC600 device, and it demonstrates the relationship between the configurations of two particles and the manipulability. Because of symmetry, we fix one particle at four different positions in one quadrant of the atomic cell, which are represented by red dots, and move the other particle in the whole atomic cell. We find that the manipulability relates to the global configurations of all particles rather than the relative distance between them. If we want to manipulate two particles in one atomic cell simultane-

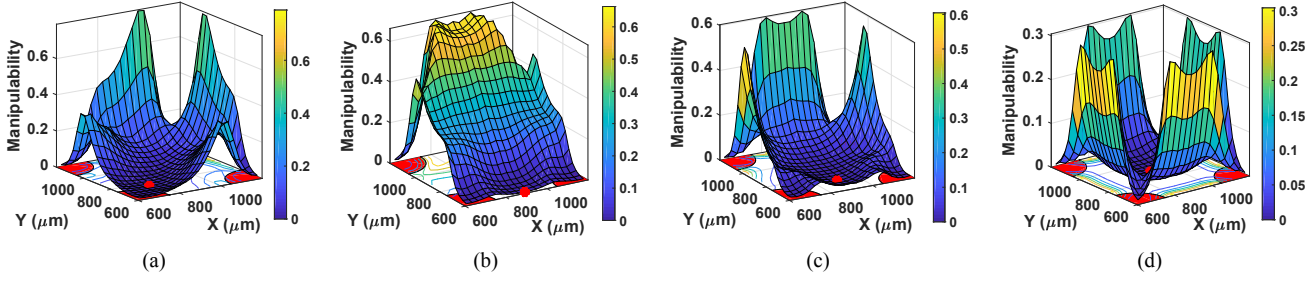


Fig. 5. Manipulability for controlling two particles in one atomic cell of a CC600 electrode array. The red dots are the positions of the fixed particle. One particle is fixed at (a)  $(757,757) \mu\text{m}$ , (b)  $(900,614) \mu\text{m}$ , (c)  $(900,728) \mu\text{m}$ , and (d)  $(900,900) \mu\text{m}$ .

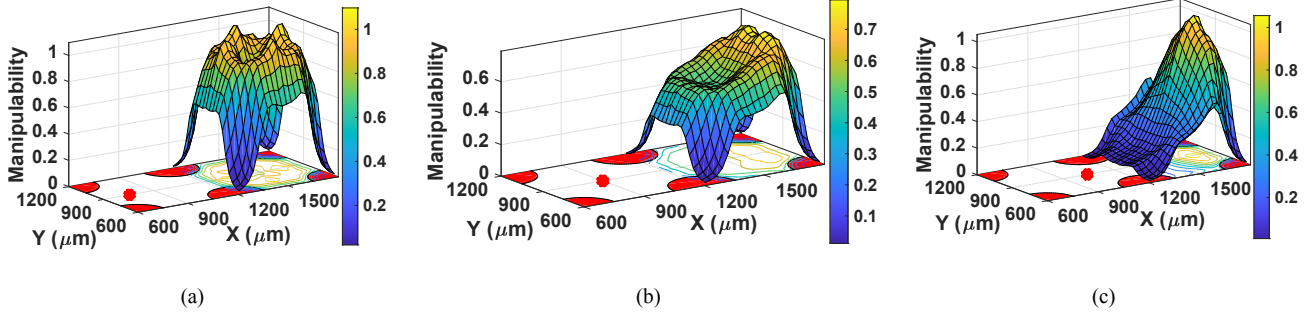


Fig. 6. Manipulability distribution for two particles in two atomic cells of a CC600 electrode array. The red dots are the positions of the fixed particle. (a) One particle is fixed at  $(757,900) \mu\text{m}$ . (b) One particle is fixed at  $(900,900) \mu\text{m}$ . (c) One particle is fixed at  $(1043,900) \mu\text{m}$ .

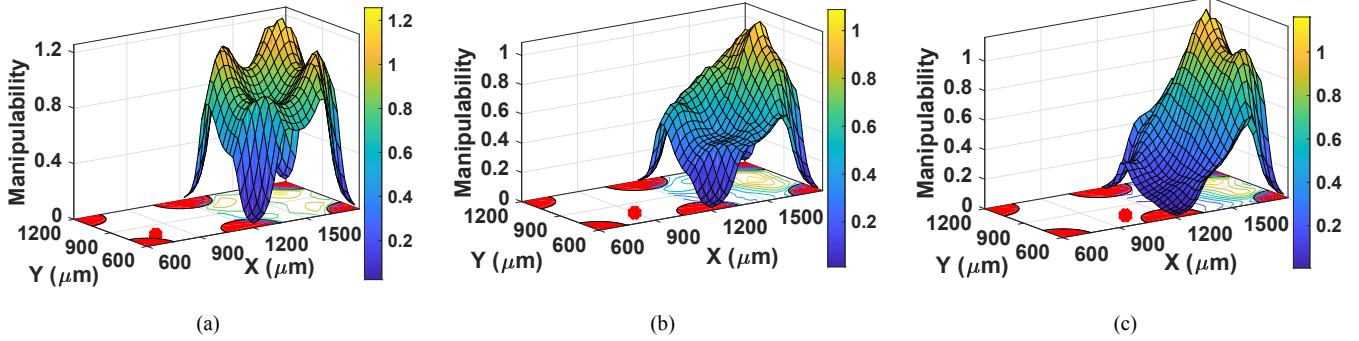


Fig. 7. Manipulability distribution for two particles in two atomic cells of a CC600 electrode array. The red dots are the positions of the fixed particle. (a) One particle is fixed at  $(757,757) \mu\text{m}$ . (b) One particle is fixed at  $(900,757) \mu\text{m}$ . (c) One particle is fixed at  $(1043,757) \mu\text{m}$ .

ously and independently, the trajectories of the particles need to be planned in the areas that achieve large manipulability, i.e., along the atomic cell boundaries. This analysis provides guidelines on testing the designed control and online motion planning algorithm in the sense of the software-in-the-loop simulations for precise, arbitrary, and independent manipulation of two particles.

#### D. Scalability analysis

We propose the generic set of  $N \times N$  lattice-shaped distributed electrodes as the actuator because we assume the electrode array can be scaled by changing  $N$ , which will allow us to scalably manipulate micro- and nanostructures. To evaluate the scalability of this pattern, we conduct manipulability simulations of controlling a particle in different atomic cells when there are no other particles in its adjacent atomic cells. The manipulability distribution in different atomic cells is identical to the manipulability distribution as shown in Fig. 4

for the same device. Therefore, the lattice pattern can be scaled up with a larger electrode number to agilely manipulate more particles if there are no particles in the adjacent atomic cells.

Figs. 6 and 7 show the manipulability distribution for two simultaneous particles in two adjacent atomic cells. Fig. 6 shows the manipulability when we fix one particle along the centerline of one atomic cell, and move the other particle in the adjacent atomic cell, and Fig. 7 illustrates the manipulability distribution of one particle in one atomic cell while the other particle is fixed closer to the edge of the adjacent atomic cell. We note that even though two particles are in two separate atomic cells, the manipulability of controlling two simultaneous particles is smaller than that for manipulating one particle and greater than putting two particles in one atomic cell. Due to the coupled electric field, it is hard to directly scale up the manipulability for multiple particles although they are in different atomic cells. To agilely manipulate multiple



simultaneous particles in adjacent atomic cells, the particles need to be kept  $L$  distance apart. The configurations of particles have a large impact on the manipulability and their trajectories need to be planned accordingly.

#### IV. EXPERIMENTAL RESULTS

In the experiments, we use the Olympus IX83 inverted microscope with a sCMOS camera to precisely locate the particles and track their movements. A LabVIEW-based real-time application integrates the position feedback from the images with the proposed controller and generates the electric fields. The  $4 \times 4$  electrode array of the microfluidic device is mounted on a PCB testing board. To verify the effect of the electrode array's CC distance on the manipulability, two devices with different dimensions are compared. One has a CC distance of  $60 \mu\text{m}$ , and the radius of the circular electrodes is  $15 \mu\text{m}$ . For the other device, the CC distance is  $600 \mu\text{m}$ , and the electrodes have a radius of  $150 \mu\text{m}$ . The influence from the particle's configuration on the manipulability is considered, so we controlled the particles at two different positions to travel to their targets with similar directions and distances to evaluate the manipulability distribution analysis.

Silicon nanowires are suspended in the heavy viscosity Drakeol 34 Mineral Oil. The lower and upper bounds of the voltage input are  $u_{\min} = 0 \text{ V}$  and  $u_{\max} = 100 \text{ V}$ , and the control step size is  $1 \text{ s}$  for one particle and  $2 \text{ s}$  for two particles because of the computational cost of optimization problems. The parameters are  $Q = I \in \mathbb{R}^{2n \times 2n}$ ,  $R = I \in \mathbb{R}^{N^2 \times N^2}$ , and  $N_h = 10$ . The target area is set to be a neighborhood with a radius of  $5 \mu\text{m}$  of the target position for each nanowire.

Fig. 8 shows the trajectories of manipulating one nanowire to its target area using the CC600 microfluidic device. Two manipulation areas are selected to compare the manipulability at different configurations. Two nanowires are controlled to reach their targets vertically below them. In Fig. 8(a), the trajectory is crossing an area with higher manipulability, while the trajectory in Fig. 8(b) lies in the area with lower manipulability. The nanowire's traveling distance in Fig. 8(a) is  $35 \mu\text{m}$ , and the total traveling time is  $46 \text{ s}$ . In Fig. 8(b), the trajectory is  $34 \mu\text{m}$  long, and the nanowire travels for  $100 \text{ s}$ . Because different nanowires have different zeta potentials, we need to consider the zeta potential when comparing the average velocities of the two nanowires. The estimated zeta potentials are  $0.042 \text{ V}$  and  $-0.032 \text{ V}$  for the nanowires in Fig. 8(a) and Fig. 8(b), respectively. Therefore, the scaled speed of the nanowire in Fig. 8(a) is  $18.05 \mu\text{m/s}$ , and the scaled speed of the nanowire in Fig. 8(b) is  $11.03 \mu\text{m/s}$ . The speed ratio is  $1.64$ , which is close to the manipulability ratio of  $1.35$  at those two configurations.

Fig. 9 are the trajectories for one nanowire using the CC60 microfluidic device. Similar to the experiments with the CC600 microfluidic device, we also select two manipulation areas to compare the manipulability at different configurations. The nanowires are moving vertically as well. In Fig. 9(a), the trajectory is within the area with higher manipulability, and the trajectory in Fig. 9(b) is in the area with lower manipulability. The traveling distance for the nanowire in Fig. 9(a) is  $30 \mu\text{m}$ ,

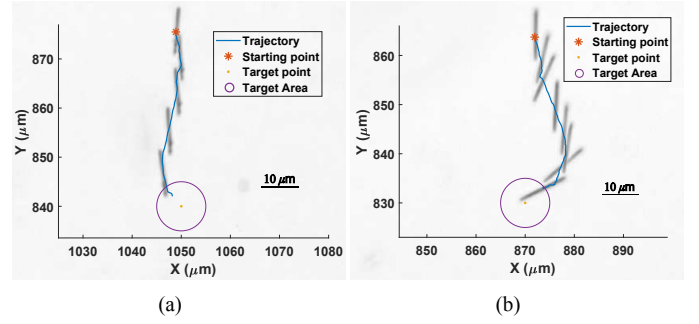


Fig. 8. Overlaid trajectory for manipulating one nanowire at the configurations with (a) higher manipulability and (b) lower manipulability.

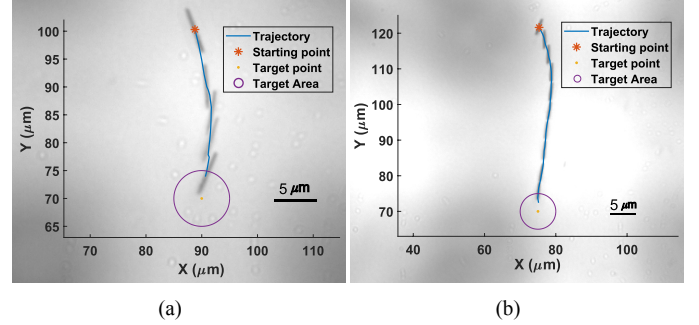


Fig. 9. (a) Overlaid trajectory for manipulating one nanowire at the configurations with (a) higher manipulability and (b) lower manipulability.

and the total traveling time is  $25.4 \text{ s}$ . In Fig. 9(b), the trajectory of the nanowire is  $51.6 \mu\text{m}$ , and the nanowire travels for  $47.8 \text{ s}$ . The estimated zeta potentials are  $-0.032 \text{ V}$  and  $-0.02 \text{ V}$  for the nanowires in Fig. 9(a) and Fig. 9(b), respectively. So the scaled speed of the nanowire in Fig. 9(a) is  $31.56 \mu\text{m/s}$ , and the scaled speed of the nanowire in Fig. 9(b) is  $44.45 \mu\text{m/s}$ . The scaled average speed magnitudes are larger than the CC600 device as indicated in the manipulability analysis.

From the experiments using two devices with different dimensions, CC600 and CC60, we note that the manipulability for the CC60 electrode array is much larger than the CC600 one. Comparing the experiments for the two dimensions, the scaled speed of the particles in the CC60 device is about  $2.86$  times faster than that in the CC600 device. According to the manipulability analysis, the ratio between the maximum manipulabilities of the CC60 and the CC600 devices is  $4$ . One possible reason is that the changing height of particles in the fluid channel affects the motion in the experiment, because the electric field strength varies in height. In the manipulability analysis, we assume that all the particles are in the same height. In future work, we will consider the height of the particles in the channel for the manipulability analysis of multiple simultaneous particles.

Next, we conduct experiments for controlling two nanowires to reach their targets independently and simultaneously. Fig. 10 in our previous work [15] shows the experimental result of manipulating two nanowires to form a horizontal line in the center atomic cell of a CC600 microfluidic device. The target positions of the two nanowires are  $120 \mu\text{m}$  distance apart. It is

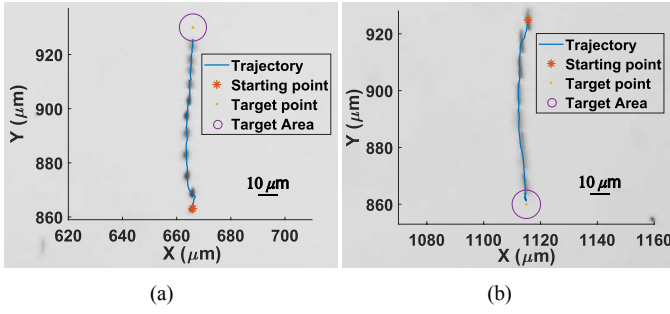


Fig. 10. Overlaid trajectories for manipulating two nanowires simultaneously along two edges of the atomic cell. (a) Trajectory for the nanowire close to the left side. (b) Trajectory for the nanowire close to the right edge.

difficult to manipulate the two simultaneous nanowires along straight lines. From our manipulability discussion, when the two nanowires are in positions close to the opposite edges of the atomic cell, larger manipulability can be achieved. Therefore, we control two nanowires simultaneously along vertical lines near the left and right boundaries of the same atomic cell in the CC600 microfluidic device. As shown in Fig. 10 of this paper, the left nanowire is moving upward and, meantime, the right one is moving downward. Due to the large distance between the two nanowires (about  $460\ \mu\text{m}$  apart), we crop the overlaid images for a clearer view of their trajectories.

We analyze the average input norm for the two experiments to evaluate the energy needed for the above manipulation. In the experiment where the two nanowires are closer to each other as shown in Fig. 10 of [15], the average voltage norm is  $296.6\ \text{V}$ , while in the case that the two nanowires are near the edges of the atomic cell as shown in Fig. 10 of this paper, the average voltage norm is  $221.1\ \text{V}$ . It indicates that when the nanowires are set along the sides, we can save about  $75\ \text{V}$  for each step. Therefore, the manipulability analyses provide us with insights to properly design the trajectories of each particle to save energy for manipulating multiple nanowires simultaneously.

## V. CONCLUSION

In this paper, we conducted comprehensive analysis and experiments to precisely manipulate single and multiple simultaneous particles under a coupled electric field in fluid suspension. We analyzed the system's manipulability based on the proposed adaptive tube MPC. In the adaptive tube MPC design, the parameter estimation method was reformulated so that multiple particles with both positive and negative zeta potentials can be manipulated simultaneously and independently. The manipulability was discussed from three aspects: the dimension of the electrode pattern, the number of the particles to be manipulated, and the configuration of the particles. Those findings complement the existing work, lead to a new device design with proper electrode dimensions, and provide insights to design achievable trajectories using online informed motion planning algorithms [21] for precise, arbitrary, and independent manipulation of multiple particles. The scalability analysis of the manipulability makes it promising

to manipulate large numbers of particles by properly putting them in different atomic cells of the  $N \times N$  electrode arrays for the application of fabricating functional nano- or microdevices. Extensive experiments shown in this work further validated the manipulability analysis. In future work, we will fabricate new devices based on our dimensional analysis, and we are working on manipulating a large number of nanowires in different atomic cells to assemble functional structures.

## REFERENCES

- [1] K. Yu, J. Yi, and J. W. Shan, "Automated characterization and assembly of individual nanowires for device fabrication," *Lab Chip*, vol. 18, no. 10, pp. 1494–1503, 2018.
- [2] S. Zhang, X. Xu, T. Lin, and P. He, "Recent advances in nano-materials for packaging of electronic devices," *J. Mater. Sci.: Mater.*, vol. 30, no. 15, pp. 13 855–13 868, 2019.
- [3] D. G. Grier, "A revolution in optical manipulation," *Nature*, vol. 424, no. 6950, pp. 810–816, 2003.
- [4] C. Gosse and V. Croquette, "Magnetic tweezers: micromanipulation and force measurement at the molecular level," *Biophys. J.*, vol. 82, no. 6, pp. 3314–3329, 2002.
- [5] D. L. Fan, F. Q. Zhu, R. C. Cammarata, and C. L. Chien, "Electric tweezers," *Nano Today*, vol. 6, pp. 339–354, 2011.
- [6] Y. L. Zhang, J. Li, S. To, Y. Zhang, X. Ye, L. You, and Y. Sun, "Automated nanomanipulation for nanodevice construction," *Nanotechnology*, vol. 23, no. 6, p. 065304, 2012.
- [7] K. Yu, J. Yi, and J. Shan, "Motion control, planning and manipulation of nanowires under electric-fields in fluid suspension," *IEEE Trans. Automat. Sci. Eng.*, vol. 12, no. 1, pp. 37–49, 2015.
- [8] —, "Simultaneous multiple-nanowire motion control, planning, and manipulation under electric fields in fluid suspension," *IEEE Trans. Automat. Sci. Eng.*, vol. 15, no. 1, pp. 80–91, 2018.
- [9] J. Wu, X. Li, and K. Yu, "Electrophoresis-Based Adaptive Manipulation of Nanowires in Fluid Suspension," *IEEE/ASME Trans. Mechatronics*, vol. 25, no. 2, pp. 638–649, 2020.
- [10] K. Yu, J. Yi, and J. W. Shan, "Real-time motion planning of multiple nanowires in fluid suspension under electric-field actuation," *Int. J. Intell. Robot. Appl.*, vol. 2, no. 4, pp. 383–399, 2018.
- [11] G. Adam, S. Chowdhury, M. Guix, B. V. Johnson, C. Bi, and D. Cappelletti, "Towards functional mobile microrobotic systems," *Robotics*, vol. 8, no. 3, p. 69, 2019.
- [12] K. Yu, X. Lu, J. Yi, and J. Shan, "Electrophoresis-based motion planning and control of nanowires in suspended fluids," in *Proc. IEEE Conf. Automat. Sci. Eng.*, Madison, WI, 2013, pp. 831–836.
- [13] C. Akin, J. Yi, L. C. Feldman, C. Durand, A.-P. Li, M. A. Filler, and J. W. Shan, "Contactless determination of electrical conductivity of one-dimensional nanomaterials by solution-based electro-orientation spectroscopy," *ACS Nano*, vol. 9, no. 5, pp. 5405–5412, 2015.
- [14] J. Wu and K. Yu, "Adaptive tube model predictive control for manipulating multiple nanowires with coupled actuation in fluid suspension," in *Proc. IFAC World Congress*, Berlin, Germany, 2020, pp. 8734–8739.
- [15] —, "Electrophoresis-based adaptive tube model predictive control of micro- and nanoparticles in fluid suspensions using global external fields," in *Proc. IEEE/ASME Int. Conf. Adv. Intell. Mechatronics*, Boston, MA, 2020, pp. 2068–2073.
- [16] C. E. Garcia, D. M. Prett, and M. Morari, "Model predictive control: theory and practice – a survey," *Automatica*, vol. 25, no. 3, pp. 335–348, 1989.
- [17] D. Q. Mayne, S. Raković, R. Findeisen, and F. Allgöwer, "Robust output feedback model predictive control of constrained linear systems," *Automatica*, vol. 42, no. 7, pp. 1217–1222, 2006.
- [18] B. T. Lopez, J. P. Howl, and J.-J. E. Slotine, "Dynamic tube MPC for nonlinear systems," in *Proc. Amer. Control Conf.*, Philadelphia, PA, 2019, pp. 1655–1662.
- [19] X. Lu and M. Cannon, "Robust adaptive tube model predictive control," in *Proc. Amer. Control Conf.*, Philadelphia, PA, 2019, pp. 3695–3701.
- [20] T. Yoshikawa, "Manipulability of robotic mechanisms," *Int. J. Robot. Res.*, vol. 4, no. 2, pp. 3–9, 1985.
- [21] X. Li and K. Yu, "Informed sampling-based motion planning for manipulating multiple micro agents using global external fields," in *Proc. IEEE Conf. Automat. Sci. Eng.*, Hong Kong, China, 2020, pp. 889–894.